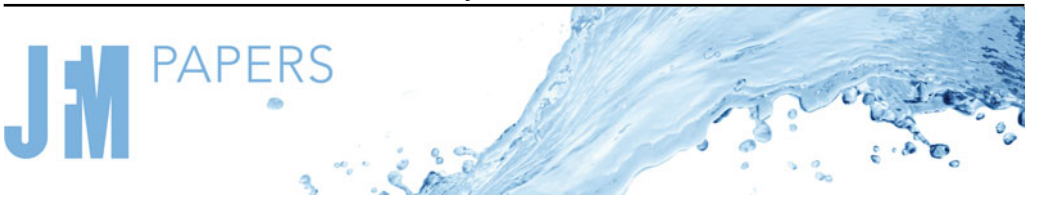
J. Fluid Mech. (2025), *vol.* 1023, A27, doi:10.1017/jfm.2025.10834



Generating the granular solitary wave

Giorgos Kanellopoulos[1], **Dimitrios Razis**[1,2,3] **and Ko van der Weele**[1]

[1]Department of Mathematics, University of Patras, 26500 Patras, Greece

[2]Mathematics Research Center, Academy of Athens, 11527 Athens, Greece

[3]Department of Physics, National & Kapodistrian University of Athens, 15771 Ilisia Athens, Greece

Corresponding author: Ko van der Weele, weele@math.upatras.gr

(Received 6 April 2025; revised 7 August 2025; accepted 10 October 2025)

Based on the generalised Saint-Venant equations for granular flow on an inclined chute, we show how to generate solitary waves from localised perturbations at the inlet. Such perturbations usually give rise to a group of roll waves, but by choosing the system parameters appropriately, the formation of all but the first wave can be suppressed, thus turning this first one into a solitary wave. This calls for a highly diffusive flow, which is realised for inclination angles close to the minimal angle required to keep the granular material flowing.

Key words: channel flow, dry granular material, solitary waves

1. Introduction

Over the past few decades, a hydrodynamic-like model has been developed to describe the flow of dry granular matter in open inclined channels. This approach features a generalised version of the Saint-Venant equations for shallow water flow, augmented by the $\mu(I)$-rheology to account for the special (non-Newtonian) frictional and diffusive properties of granular materials (Forterre & Pouliquen 2003; GDR-MiDi 2004; Yop *et al.* 2005, 2006; Gray & Edwards 2014; Baker, Barker & Gray 2016). A number of studies have successfully adopted this approach to capture the dynamics of various waveforms, including travelling and standing waves, erosion-deposition waves and granular avalanches (Forterre 2006; Gray & Cui 2007; Di Cristo *et al.* 2009; Johnson & Gray 2011; Gray & Edwards 2014; Razis *et al.* 2014; Edwards & Gray 2015; Edwards *et al.* 2017; Viroulet *et al.* 2017, 2018; Razis, Kanellopoulos & van der Weele 2019; Rocha, Johnson & Gray 2019; Russell *et al.* 2019; Edwards *et al.* 2021; Kanellopoulos, Razis & van der Weele 2021; Kanellopoulos 2021; Kanellopoulos, Razis & van der Weele 2022; Edwards *et al.* 2023; Razis, Kanellopoulos & Van der Weele 2023; Kanellopoulos, Razis & van der Weele 2024; Kanellopoulos 2025). One waveform, however, has remained relatively unexplored:

© The Author(s), 2025. Published by Cambridge University Press. This is an Open Access article, distributed under the terms of the Creative Commons Attribution-NonCommercial-ShareAlike licence (https://creativecommons.org/licenses/by-nc-sa/4.0/), which permits non-commercial re-use, distribution, and reproduction in any medium, provided the same Creative Commons licence is used to distribute the re-used or adapted article and the original article is properly cited. The written permission of Cambridge University Press or the rights holder(s) must be obtained prior to any commercial use.

https://doi.org/10.1017/jfm.2025.10834 Published online by Cambridge University Press

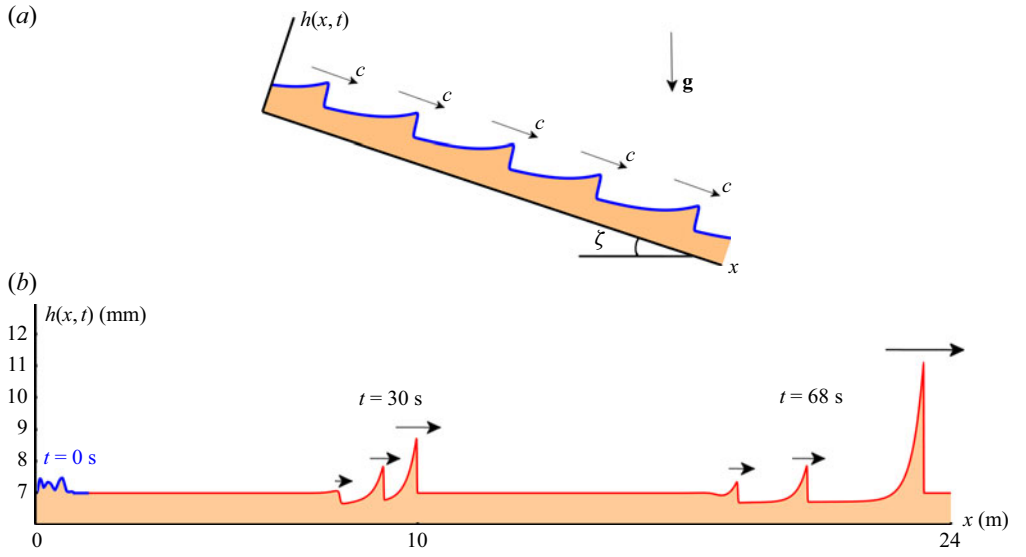


Figure 1. (*a*) A periodic train of fully ripened granular roll waves, propagating with speed c along a chute inclined at an angle ζ. Roll waves are the dominant travelling waveform when the Froude number Fr exceeds a critical value Fr_{cr} as defined by (2.6). To highlight the typical shape of the roll waves, only the upper part of the granular sheet (close to the free surface) has been depicted and the vertical scale has been greatly expanded. In reality, the wavelength of these waves is much larger than the height of the sheet, which in turn is significantly larger than the wave amplitude. (*b*) Successive stages in the development of a group of roll waves caused by a localised initial perturbation (blue) at the top of the chute. For economy of space, here – and in all figures to follow – the chute has been depicted horizontally with the understanding that it is actually tilted by an angle ζ.

the solitary wave. To the best of our knowledge, it is an open question whether flowing granular sheets can sustain such a wave. Hitherto, solitary granular waves have been reported in theoretical studies by Razis *et al.* (2019) (see especially figure 8*c* therein) and Kanellopoulos *et al.* (2022) (see figure 9 therein), but these waves required an unrealistic amount of fine tuning of the system parameters and, in addition, their stability was questionable. In this paper, we follow a different route and the solitary waves in question are sufficiently robust to make their detection in experiments feasible: we establish the conditions under which a localised perturbation of the flow gives rise to one single roll wave. Usually, this type of perturbation generates a whole group of roll waves. By tuning the system parameters, however, the formation of all but the first roll wave can be suppressed for arbitrarily long times. This means that – on any chute of finite length – the leading roll wave will remain solitary.

Roll waves form spontaneously when the Froude number Fr of the incoming flow at the top of the chute exceeds a certain critical value Fr_{cr} (to be specified in § 2). Beyond this threshold, the uniform flow is unstable. Small perturbations on the surface of the flowing sheet are amplified and grow, given time, into a periodic train of roll waves (Savage & Hutter 1989; Forterre & Pouliquen 2003; Gray & Edwards 2014; Razis *et al.* 2014; Edwards & Gray 2015; Razis *et al.* 2019; Fei *et al.* 2021; Kanellopoulos *et al.* 2022; Razis *et al.* 2023). The formation of such a train, however, is a multi-step procedure in which the larger (and therefore faster) travelling perturbations overtake the smaller (and thus slower) ones. In this way, the larger perturbations grow at the expense of the smaller ones, and begin to resemble roll waves with their characteristic steep front and long, gradually diminishing tail. This coarsening process continues – if the chute is long enough – until the waves reach equal size, at which point the coarsening is arrested, as described by Razis *et al.* (2014). Figure 1(*a*) shows such a fully ripened roll wave train.

https://doi.org/10.1017/jfm.2025.10834 Published online by Cambridge University Press

The above-mentioned scenario holds when the roll waves are allowed to develop spontaneously from the naturally occurring tiny perturbations (on the surface of the uniform flow) along the entire length of the channel. One may also generate roll waves by expressly introducing not-so-tiny disturbances at the top of the chute, e.g. by repeatedly raising and lowering the inlet for a short time interval. This is a technique that was used by Brock (1967) and more recently by Yu & Chu (2022) to create roll waves in a water channel. These authors found that the disturbance at the inlet of the channel first generates a series of well-separated roll waves consisting of an exceptionally large front runner and several trailing waves of successively smaller amplitude and wavelength; see figure 1(*b*) for a similar observation in the granular flow studied in the present paper. In the wake of this initial series of waves, when the amplitude and wavelength have fallen to their final values, the standard periodic train of roll waves establishes itself (Yu & Chu 2022).

Here, we employ the same method to generate roll waves on a chute with granular matter, and moreover, we specify the conditions under which the second and subsequent waves are suppressed to such a degree that the front runner will effectively travel alone. It will exit the end of any finite chute before the second wave is generated and, in this way, the front runner manifests itself as the sought-after granular solitary wave.

The paper is organised as follows. In § 2, the governing equations are given, being the generalised Saint-Venant equations for granular channel flow, together with the closure relations for the friction exerted by the chute on the flowing material and for the diffusive forces arising from the in-plane stresses within the sheet. Here, we also present the non-dimensional formulation of the model and the numerical scheme used to solve the equations. Section 3 then describes in detail how the granular solitary wave is produced and we show that its wave speed is in good agreement with the analytical prediction by Razis *et al.* (2014). Section 4 discusses the effect of varying the system parameters, providing a road map for generating such a wave in actual experiment. Finally, § 5 summarises our results.

2. Governing equations

2.1. *Generalised Saint-Venant equations for granular flow*

The fact that the wavelength of the roll waves is much larger than the height of the sheet, which in turn is significantly larger than the amplitude of the waves (see the caption of figure 1), justifies the use of an analysis similar to the shallow water approximation for open channel flow. The relevant quantities for this approach are the sheet's height, $h(x,t)$, and the average velocity, $\bar{u}(x,t)$, defined as

$$\bar{u}(x,t) = \frac{1}{h(x,t)} \int_0^{h(x,t)} u(x,z,t)\,\mathrm{d}z, \tag{2.1}$$

where $u(x,z,t)$ is the detailed velocity profile along the vertical cross-section of the sheet. Any variations in the y-direction (from side to side of the channel) are ignored.

The dynamics of the sheet can then be described by two coupled, nonlinear partial differential equations governing $h(x,t)$ and $\bar{u}(x,t)$ (Gray & Edwards 2014; Razis *et al.* 2014; Edwards & Gray 2015; Edwards *et al.* 2017; Razis *et al.* 2018, 2019):

$$\frac{\partial h}{\partial t} + \frac{\partial}{\partial x}(h\bar{u}) = 0, \tag{2.2}$$

$$\frac{\partial}{\partial t}(h\bar{u}) + \frac{\partial}{\partial x}(h\bar{u}^2) = gh\sin\zeta - \frac{\partial}{\partial x}\left(\frac{1}{2}gh^2\cos\zeta\right) - \mu(h,\bar{u})gh\cos\zeta + \frac{\partial}{\partial x}\left(\nu(\zeta)h^{3/2}\frac{\partial \bar{u}}{\partial x}\right), \tag{2.3}$$

https://doi.org/10.1017/jfm.2025.10834 Published online by Cambridge University Press

which represent the mass conservation within the sheet and the momentum balance, respectively. Here, it should be noted that, following the approach of Savage & Hutter (1989), the granular material is treated as an incompressible fluid, with a constant density that has been divided out of equations (2.2) and (2.3). The equations also reflect the fact that we confine our attention to the (x, z)-plane and that any transport in the cross-wise direction is neglected.

The left-hand side of (2.3) expresses the rate of change (i.e. the Stokesian derivative) of the depth-averaged momentum. The right-hand side contains the various forces integrated across the sheet's depth. In order of appearance: (i) the gravitational component acting in the direction of the flow (x-direction); (ii) the pressure gradient arising from variations in the sheet's height $h(x, t)$; (iii) the frictional resistance exerted by the chute's surface, modelled by a friction coefficient $\mu(h, \bar{u})$ (which depends on both height and velocity) multiplied by the normal force acting on the sheet; and finally, (iv) a diffusive term accounting for the net effect of the in-plane stresses within the sheet, averaged across its depth, which overall behaves very much like a viscous force despite its nonlinear form and the fact that $\nu(\zeta)$ is expressed in $\mathrm{m}^{3/2}\ \mathrm{s}^{-1}$, which is different from the usual dimensions ($\mathrm{m}^2\ \mathrm{s}^{-1}$) of a viscosity coefficient. Both $\mu(h, \bar{u})$ and $\nu(\zeta)$, which account for the specific frictional and diffusive characteristics of granular materials, are derived on the grounds of what is now known as the $\mu(I)$-rheology (Pouliquen & Forterre 2002; GDR-MiDi 2004).

Regarding the friction coefficient $\mu(h, \bar{u})$, we use the following expression from Edwards *et al.* (2017):

$$\mu(h, \bar{u}) = \tan\zeta_1 + (\tan\zeta_2 - \tan\zeta_1)\left(1 + \frac{\beta h}{\mathcal{L}(Fr + \Gamma)}\right)^{-1}, \tag{2.4}$$

where ζ_1, ζ_2, $\mathcal{L}$, β and Γ are experimentally determined parameters, and Fr is the Froude number of the flow.

The inclination angles ζ_1 and ζ_2 define the bounds between which the chute can sustain a uniform flow. If the inclination angle of the chute (ζ) is less than ζ_1, the granular sheet remains immobile. Conversely, if ζ is larger than ζ_2, the sheet avalanches downwards in an accelerated fashion.

The length scale $\mathcal{L}$ is an experimental fit parameter, typically of the order of a few particle diameters (Pouliquen & Forterre 2002; Edwards *et al.* 2017). The parameters β and Γ are dimensionless constants introduced to make (2.4) amendable to the measured data for a variety of materials. The constant Γ represents an offset of the Froude number, making the friction law also applicable to the flow of rough particles. The precise values of $\mathcal{L}$, β and Γ depend on the physical properties of the granular material used as well as on the roughness of the underlying surface.

Edwards *et al.* (2017) introduced an additional parameter β_*, being the Froude number of the thinnest possible uniform flow. The latter is determined experimentally by measuring the thickness of the residual layer which is left on the chute after the supply at the inlet has been turned off and the surplus of granular material has been allowed to flow out of the system. The specific values of β_* given in table 1 have been taken from the relevant publications by Russell *et al.* (2019) for glass beads, Edwards *et al.* (2019) for carborundum particles and Edwards *et al.* (2023) for fine sand.

As long as $Fr(x, t) \geqslant \beta_*$ everywhere along the chute, the granular flow will remain fully dynamic (Edwards *et al.* 2017), with the Froude number $Fr(x, t)$ being defined as

$$Fr(x, t) = \frac{\bar{u}(x, t)}{\sqrt{h(x, t) g \cos\zeta}}. \tag{2.5}$$

https://doi.org/10.1017/jfm.2025.10834 Published online by Cambridge University Press

	ζ_1 (deg)	ζ_2 (deg)	d (mm)	$\mathcal{L}$ (mm)	β	β_*	Γ	Fr_{cr}
(i)	21.3	33.9	0.13–0.16	0.24	0.14	0.19	0.00	0.667
(ii)	31.1	47.5	0.28–0.35	0.44	0.63	0.47	0.40	0.400
(iii)	29.0	45.5	0.45	0.90	0.71	0.11	0.84	0.107

Table 1. Experimentally obtained parameter values used in the numerical simulations, concerning the flow of three different materials over channels with glass beads glued to the bottom: (i) glass beads (Russell *et al.* 2019); (ii) carborundum particles (Edwards *et al.* 2019); and (iii) fine sand (Edwards *et al.* 2023). The symbol d signifies the (mean) particle diameter. In all simulations, we use $g = 9.81$ m s^{-2}.

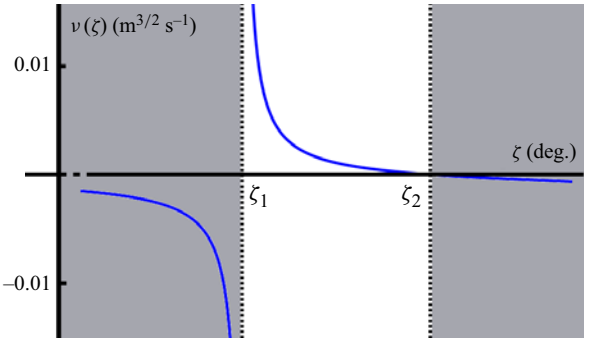


Figure 2. Coefficient $\nu(\zeta)$ of the diffusive term in (2.3) as a function of ζ, see (2.7). The regions outside the interval $\zeta_1 < \zeta < \zeta_2$ are shaded to indicate that the $\mu(I)$-rheology on which the evaluation of $\nu(\zeta)$ is based becomes ill-posed there. For the construction of this plot, the numerical values of the parameters featuring in $\nu(\zeta)$ are those of table 1, set (iii). The parameter sets (i) and (ii) yield qualitatively similar plots.

Also, for $Fr \geqslant Fr_{cr}$, the uniform flow becomes unstable and gives way to roll waves, where the critical Froude number is given by (Forterre & Pouliquen 2003; Kanellopoulos 2021)

$$Fr_{cr} = \frac{2}{3}(1 - \Gamma), \tag{2.6}$$

which depends only on the aforementioned Froude offset Γ. So, to generate roll waves, one has to ensure that the Froude number exceeds both β_* and Fr_{cr}, i.e. $Fr(x, t) > max(\beta_*, Fr_{cr})$.

Regarding the second key parameter in the momentum balance (2.3), the coefficient $\nu(\zeta)$ of the diffusive term, we employ the analytic expression derived by Gray & Edwards (2014) building upon earlier work by Forterre (2006):

$$\nu(\zeta) = \frac{2\mathcal{L}\sqrt{g}\sin\zeta}{9\beta\sqrt{\cos\zeta}}\,\gamma(\zeta), \quad \text{where } \gamma(\zeta) = \frac{\tan\zeta_2 - \tan\zeta}{\tan\zeta - \tan\zeta_1}. \tag{2.7}$$

This coefficient $\nu(\zeta)$, which will play an important role in our method for generating solitary waves, is depicted in figure 2. It should be noted that (2.7) is only valid within the range of inclination angles where steady uniform flows are possible, i.e. for $\zeta_1 < \zeta < \zeta_2$. Outside this range, (2.7) takes on negative values and the diffusive term would no longer act as a levelling mechanism, but rather as a term that would enhance the height differences in the sheet; this can be attributed to the ill-posedness of the $\mu(I)$-rheology below ζ_1 and above ζ_2. At the lower critical angle ($\zeta = \zeta_1$), the value of $\nu(\zeta)$ approaches infinity, while at the upper critical angle ($\zeta = \zeta_2$), it becomes zero.

To conclude this section, we note that under uniform flow conditions, i.e. $h(x, t) = h_0$ and $\bar{u}(x, t) = \bar{u}_0$, the mass balance (2.2) is trivially satisfied and the momentum balance

https://doi.org/10.1017/jfm.2025.10834 Published online by Cambridge University Press

(2.3) reduces to $\tan\zeta = \mu(h_0, \bar{u}_0)$. This implies (Kanellopoulos 2021)

$$h_0 = \frac{\mathcal{L}\gamma(\zeta)}{\beta}\,(Fr_0 + \Gamma), \quad \bar{u}_0 = \frac{\beta\sqrt{g\cos\zeta}}{\mathcal{L}\gamma(\zeta)}\,h_0^{3/2} - \Gamma\sqrt{g\cos\zeta}\,h_0^{1/2}, \tag{2.8}$$

where Fr_0 is the Froude number of the uniform flow in question. This will be the base flow on which we will impose the local perturbation at the inlet to generate roll waves.

2.2. *Non-dimensional formulation*

The model for granular flow presented in the previous subsection can be cast in non-dimensional form by expressing all length scales (both the position x along the chute and the height $h(x,t)$ of the sheet) in terms of the thickness h_0 of the uniform base flow. A natural choice for the unit of time then is $h_0/\bar{u}_0$, so the non-dimensional variables become $\tilde{x} = x/h_0$ and $\tilde{t} = t/(h_0/\bar{u}_0)$, where tildes denote non-dimensional quantities. The height and depth-averaged velocity are thus rescaled as follows:

$$\tilde{h} = \frac{h}{h_0}, \quad \tilde{\bar{u}} = \frac{\bar{u}}{\bar{u}_0}. \tag{2.9}$$

The mass balance (2.2) proves to be invariant for this transformation and now reads

$$\frac{\partial\tilde{h}}{\partial\tilde{t}} + \frac{\partial}{\partial\tilde{x}}(\tilde{h}\tilde{\bar{u}}) = 0, \tag{2.10}$$

whereas the momentum balance (2.3) takes the following form (Kanellopoulos *et al.* 2022):

$$Fr_0^2\left(\frac{\partial}{\partial\tilde{t}}(\tilde{h}\tilde{\bar{u}}) + \frac{\partial}{\partial\tilde{x}}(\tilde{h}\tilde{\bar{u}}^2)\right) = \tilde{h}\big(\tan\zeta - \mu(\tilde{h},\tilde{u})\big) - \tilde{h}\frac{\partial\tilde{h}}{\partial\tilde{x}} + \frac{Fr_0^2}{R_0}\frac{\partial}{\partial\tilde{x}}\left(\tilde{h}^{3/2}\frac{\partial\tilde{\bar{u}}}{\partial\tilde{x}}\right), \tag{2.11}$$

where Fr_0 is the Froude number of the uniform base flow and R_0 is the granular analogue of the Reynolds number introduced by Gray & Edwards (2014), again defined in terms of the base flow quantities:

$$R_0 = \frac{\bar{u}_0\sqrt{h_0}}{\nu(\zeta)}. \tag{2.12}$$

Naturally, also the friction coefficient μ must, in this context, be expressed as a function of the new dimensionless parameters:

$$\mu(\tilde{h},\tilde{\bar{u}}) = \tan\zeta_1 + (\tan\zeta_2 - \tan\zeta_1)\left(1 + \frac{\beta h_0\tilde{h}}{\mathcal{L}\left(\Gamma + Fr_0(\tilde{\bar{u}}/\sqrt{\tilde{h}}\,)\right)}\right)^{-1}. \tag{2.13}$$

Noting that the velocity $\bar{u}_0$ is related to the height h_0 via (2.8), the Froude number Fr_0 and the granular Reynolds number R_0 can be expressed as functions of h_0 alone, and are in fact related to each other (Razis *et al.* 2019; Kanellopoulos 2021):

$$Fr_0 = \frac{\beta h_0}{\mathcal{L}\gamma(\zeta)} - \Gamma, \quad R_0 = \frac{\mathcal{L}\gamma(\zeta)\sqrt{g\cos\zeta}}{\beta\nu(\zeta)}\,Fr_0(Fr_0 + \Gamma), \tag{2.14}$$

which means that the granular Reynolds number R_0 can be eliminated from (2.11), leaving only Fr_0 and ζ as the two relevant dimensionless numbers governing granular chute flow. Equation (2.14) for Fr_0 shows that, for fixed ζ, an increase of h_0 results in a higher Froude number.

https://doi.org/10.1017/jfm.2025.10834 Published online by Cambridge University Press

Despite the elegance of the non-dimensional formulation, it turns out that the original dimensional form of the model is more suitable for numerically solving the equations. This will be explained in the next subsection.

2.3. *Numerical scheme*

To numerically integrate the two governing equations (2.2)–(2.3), we use the 'method of lines' (Schiesser 1991; Hamdi, Schiesser & Griffiths 2007), which has also been employed in previous publications of our group to capture a variety of waveforms observed in granular chute flow (Razis *et al.* 2018, 2019; Kanellopoulos *et al.* 2021; Kanellopoulos 2021; Kanellopoulos *et al.* 2022). This method turns the two partial differential equations (PDEs) into a system of many ordinary differential equations (ODEs). This is achieved by discretising the spatial variable x in small steps of a fixed length Δx (resulting in a uniform grid $0 \leqslant x_i \leqslant x_{max}$) and employing a central-difference scheme to approximate the spatial derivatives, leaving t as the only continuous independent variable. The number of ODEs to be solved then consists of $x_{max}/\Delta x + 1$ equations per PDE, amounting to a system of twice as many coupled ODEs. To produce the figures in the present paper, we have used a variety of grid spacings from $\Delta x = 0.00055$ to $\Delta x = 0.003$, depending on the length of the chute (x_{max}) and the required accuracy. In each case, the step size was optimised to guarantee that the profiles obtained were free of grid-dependent artefacts. As an extra confirmation, in each run, we checked that the area under the profile of $h(x, t)$ was conserved in agreement with the mass balance in the system.

This system of ODEs – with appropriate initial conditions $h(x, 0)$ and $\bar{u}(x, 0)$ – via the so-called LSODA algorithm, which uses the Adams method for non-stiff regions and, whenever stiffness is detected, switches to a variable-step, variable-order Backwards Difference formula. Thanks to the presence of the diffusion, however, stiffness never occurred.

Here, we note that, especially in the case of roll waves, the computational demands are high. To resolve this, we used the 'restart technique', in which the total simulation time is divided in smaller intervals. We run the system for the first time interval and use the output at the end of the interval as initial conditions for the second run, and so on. An added benefit of this technique is that the duration of the time interval is adjustable, so it can be shortened (and the grid spacing Δx can be refined) when more accuracy is required.

Evidently, when x_{max} becomes larger, one needs more space steps to maintain the desired accuracy. In non-dimensional units, the length of the chute is expressed as a multiple of the tiny height h_0 and, thus, $\tilde{x}_{max}$ will typically become enormous. This is the reason why we choose to work with the dimensional equations (where the length x_{max} is expressed in metres) in all our numerical simulations.

3. Creating the granular solitary wave

3.1. *Generating a group of roll waves*

As mentioned in § 1, the method we employ for generating a group of roll waves is to apply perturbations locally at the inlet of the chute (and nowhere else). In practice, this can be achieved by randomly varying the height of the entrance gate for a certain time interval. Figure 3 illustrates such a numerical simulation, where we have adopted parameter values taken from an actual experiment involving flowing sand over a bed of glass beads (Rocha *et al.* 2019; Edwards *et al.* 2023); see table 1, set (iii). Most of the results shown in this paper are for this parameter set, yet we have corroborated the general validity of our findings by also performing simulations with the parameter sets (i) and (ii), see § 4.

https://doi.org/10.1017/jfm.2025.10834 Published online by Cambridge University Press

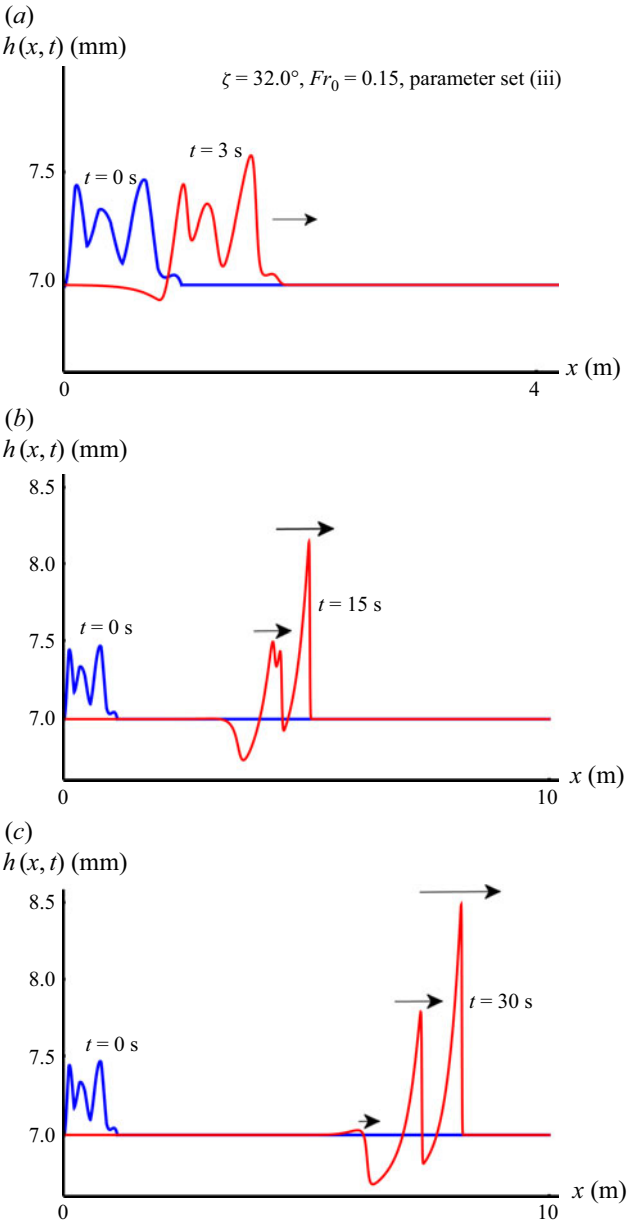


Figure 3. Numerical simulation showing the first stages of the formation of a roll wave pattern due to a localised initial perturbation at the inlet (blue). The red profiles show the flow configuration after (*a*) $t = 3$ s, (*b*) $t = 15$ s and (*c*) $t = 30$ s. The parameter values used in the simulation are those of table 1, set (iii); the inclination angle of the chute is $\zeta = 32.0°$ (between ζ_1 and ζ_2) and the Froude number of the base flow is $Fr_0 = 0.15 > \beta_* > Fr_{cr}$.

In figure 3, we have chosen the inclination angle to be $\zeta = 32.0°$ (the same value as the one adopted by Rocha *et al.* (2019)) and the Froude number of the base flow $Fr_0 = 0.15$, which exceeds the critical value $Fr_{cr} = (2/3)(1 - \Gamma) = 0.107$, to guarantee that the uniform base flow will be unstable and thus prone to the formation of roll waves. This unstable base flow, in accordance with the expressions given in (2.8), has thickness $h_0 = 6.98$ mm and depth-averaged velocity $\bar{u}_0 = 0.036$ m s^{-1}. On top of this flow,

https://doi.org/10.1017/jfm.2025.10834 Published online by Cambridge University Press

we impose a random positive perturbation along the first metre of the chute, indicated by the blue profile in figure 3. This then is the initial condition we use for numerically solving the Saint-Venant equations (2.2) and (2.3).

To facilitate a direct comparison between the numerical experiments throughout the paper, we implement the same initial condition in all of the runs (except those of figure 8, where we will discuss the fact that the resulting waves are quite insensitive to the specific shape of the perturbation at the inlet), properly scaled to fit the proportions of the flow in each simulation. The procedure is illustrated in figure 3(*a*): we generate a prototype random non-dimensional perturbation $\eta(x)$, adjust its amplitude in proportion to the value of h_0 of the flow under study and then superpose it to the base flow on the first metre of the chute. So, the initial profile takes the form

$$h(x,0) = \begin{cases} h_0(1+\eta(x)) & \text{for} \quad 0\,\text{m} \leqslant x \leqslant 1\,\text{m}, \\ h_0 & \text{for} \quad x \geqslant 1\,\text{m}. \end{cases} \tag{3.1}$$

The perturbation $\eta(x)$ is a continuous and differentiable function, created by interpolating the discrete heights of the random profile via Hermite polynomials. In particular, at $x = 1$ m, the perturbed profile on the first metre connects smoothly to the uniform level h_0 for $x > 1$ m. Moreover, in all our runs (with the exception of supplementary movie 1 available at https://doi.org/10.1017/jfm.2025.10834), we stop the simulation before the first waves reach the exit of the system; hence, the boundary condition at $x = x_{max}$ is simply $h(x_{max}, t) = h_0$, $\bar{u}(x_{max}, t) = \bar{u}_0$, $\partial\bar{u}(x_{max}, t)/\partial x = 0$.

Figure 3(*a*) shows the profile of the granular sheet after $t = 3$ s (red curve). We see that the added material travels downstream, with the leading peak visibly gaining amplitude, and the formation of a valley at the trailing edge of the group.

In figure 3(*b*), at $t = 15$ s (red curve), the leading peak has evolved into a large-amplitude front runner. With its steep front and gradually falling tail, it has already assumed the familiar shape of a roll wave. The two peaks following are caught in the act of merging. Such merging events constitute the basic mechanism of the coarsening process via which the flow creates the characteristic roll wave pattern: higher waves are faster and thus catch up with lower (and therefore slower) waves in front of them (Razis *et al.* 2014). Meanwhile, the roll waves grow in size at the expense of the base flow by carving valleys into the granular sheet, i.e. regions where $h(x, t) < h_0$.

In figure 3(*c*), at $t = 30$ s, the aforementioned merging is complete and now also the second wave has assumed the characteristic shape of a roll wave. The waves have increased in amplitude and thus in velocity, and moreover, at the trailing edge of the wave group, we witness the birth of a third wave. Here, the incoming flow (with depth-averaged velocity $\bar{u}_0$) meets the valley where $\bar{u} < \bar{u}_0$, and this causes the incoming flow to create an upheaval here, which will eventually develop into a third roll wave. Clearly, the ripening of the wave group is still in progress, yet the three stages shown here already give a good picture of the dynamics of the process. More extensive simulations show that the resulting pattern – a group of travelling roll waves – is a very generic one, independent of the exact details of the initial perturbation and qualitatively the same also for other granular materials.

The observed wave speeds at the end of the simulation are found to agree very well with the analytical prediction of Razis *et al.* (2014). Based on the fact that mass must be conserved across the steep front of the roll wave, and momentum very nearly so, these authors showed that the wave speed c of a roll wave as a function of its peak height h_p is given by the approximative expression

$$c(h_p) = \bar{u}_0 + \sqrt{\frac{1}{2} g \cos\zeta \left(1 + \frac{h_p}{h_0}\right) h_p}. \tag{3.2}$$

https://doi.org/10.1017/jfm.2025.10834 Published online by Cambridge University Press

To illustrate the agreement between simulation and theory, we mention that the front runner in figure 3(*c*), with peak height $h_p = 8.52$ mm, was numerically measured to propagate at a speed $0.3193\ \mathrm{m\,s^{-1}}$, whereas the analytical relation (3.2) gives a wave speed $c(h_p) = 0.3179\ \mathrm{m\,s^{-1}}$.

Equation (3.2) was derived in the context of granular chute flow, but it is in fact valid also for roll waves in standard fluids. This is because the diffusive term at the end of (2.3) is left out of the derivation because of its smallness, and the frictional losses over the very short interval of the wave front are assumed to be negligible. That is to say, the two terms in (2.3) containing the specific characteristics of the granular rheology have only a minor influence on the relation between the peak height and the wave speed, and they do not affect (3.2).

3.2. *Making the front runner solitary*

The results of the previous subsection suggest a method for generating a solitary wave, namely, to suppress the formation of the second wave (and all subsequent waves) while keeping the front runner intact. This will make the front runner for all practical purposes a solitary wave.

Our strategy for achieving this is to adjust the inclination angle ζ of the chute as well as the Froude number Fr_0 of the base flow. The angle ζ should be chosen close to the minimal value ζ_1 (where the coefficient $\nu(\zeta)$ becomes large, cf. figure 2) to enhance the diffusive effects in the flow, thereby suppressing the growth of height fluctuations. Naturally, this will affect not only the second and subsequent waves, but also the front runner. Therefore, we need to adjust also the Froude number Fr_0 in such a way as to ensure that the flow is sufficiently energetic to let the front runner maintain a substantial amplitude, but not energetic enough to permit the appearance of less prominent waves.

We will take $\zeta = 29.5°$, just half a degree above ζ_1, for which $\nu(\zeta) = 18.4 \times 10^{-3}\ \mathrm{m^{3/2}\,s^{-1}}$ (against $\nu(\zeta) = 2.8 \times 10^{-3}\ \mathrm{m^{3/2}\ s^{-1}}$ for $\zeta = 32.0°$), cf. (2.7). To check the pure effect of this parameter change, we will, in the first instance, keep Fr_0 equal to its value in the previous simulation, i.e. $Fr_0 = 0.15$. The height and depth-averaged velocity of the base flow corresponding to these values of ζ and Fr_0 are $h_0 \simeq 49.5$ mm (seven times as high as previously) and $\bar{u}_0 \simeq 0.0975\ \mathrm{m\,s^{-1}}$, respectively, as given by (2.8). For the sake of comparison, the initial condition used is the same localised perturbation as before, only scaled up in proportion to the thickness of the base flow h_0. The results of the numerical simulation are shown in figure 4, where the blue curve again represents the initial perturbation.

Figure 4(*a*) shows the flow profile after $t = 3$ s (red curve). The perturbations are travelling downstream considerably faster than in the previous simulation (see figure 3*a*) and are in fact already forming one travelling compound propagating downstream. In this context, we note that the diffusive effect of the term $\nu(\zeta)(h^{3/2}\bar{u}_x)_x$ in the momentum balance (2.3) makes itself especially felt during the very early stages of the evolution, when the expression $(h^{3/2}\bar{u}_x)_x$ attains large values due to the sharp height and velocity variations of the random perturbations. As a consequence, the length scale below which perturbations are smoothed out is enhanced by the increased value of $\nu(\zeta)$, and any details of the profile at smaller scales will vanish. This is exactly what one witnesses in figure 4(*a*): only the most coarse-grained features of the initial perturbation survive.

An equivalent way of saying this is that the so-called 'cut-off frequency' – which owes its existence to the presence of the diffusive term (Forterre & Pouliquen 2003; Gray & Edwards 2014; Razis *et al.* 2014) and which sets the critical frequency above which the growth rate of instabilities becomes negative – is lowered by the stronger diffusion.

In figure 4(*b*), after $t = 15$ s, thanks to the levelling effect of the enhanced diffusion in the flow, the compound of the previous plot has lost even more of its detail and has

https://doi.org/10.1017/jfm.2025.10834 Published online by Cambridge University Press

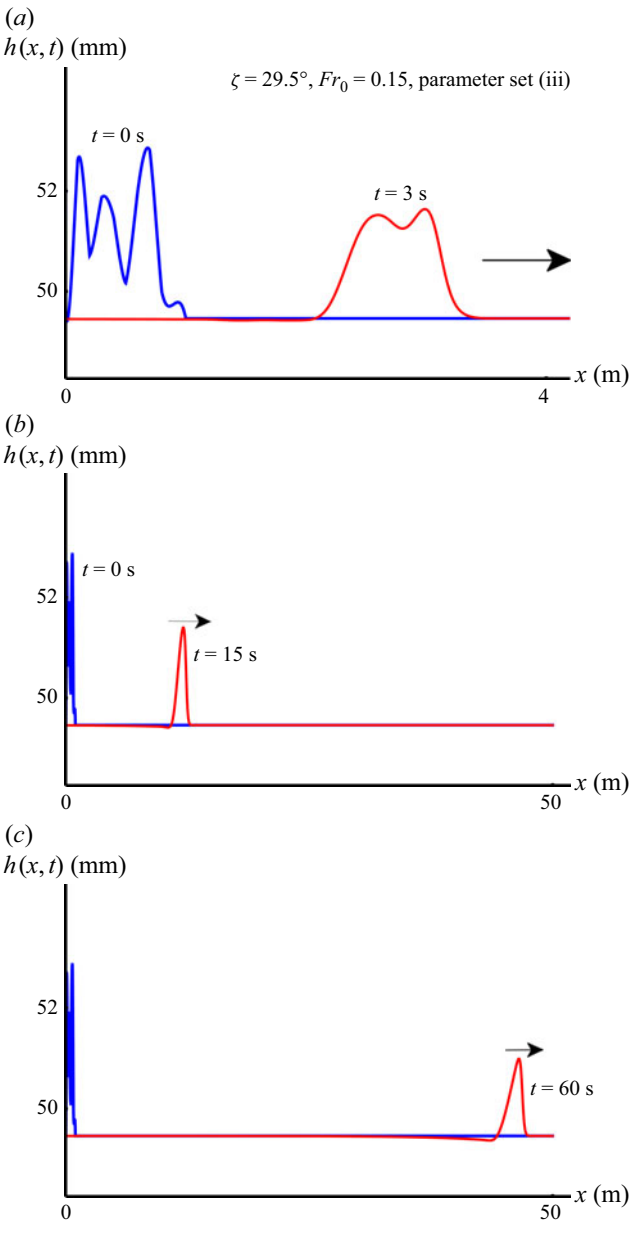


Figure 4. Numerical experiment for a smaller inclination angle ($\zeta = 29.5°$), while $Fr_0 = 0.15$ is the same as in figure 3. The initial condition (blue) is identical to that of figure 3, only scaled up to comply with the increased thickness of the base flow. The red profiles show the flow at (*a*) $t = 3$ s, (*b*) $t = 15$ s and (*c*) $t = 60$ s. Note that the length of the chute is five times as long as in figure 3. The parameter values used are those of table 1, set (iii).

become a single peak. By now, it is clear that no other waves are emerging from the initial perturbation.

In figure 4(*c*), at $t = 60$ s, we observe that this solitary peak has persisted and travelled a significant distance ($x = 50$ m). It has assumed the familiar shape of a roll wave, with a steep front and gently sloping tail, and it has carved out a shallow valley. The speed of this front runner (with peak height $h_p = 51.07$ mm) is numerically found to be $0.7644\ \mathrm{m\,s^{-1}}$, in excellent agreement with the predicted value $c(h_p) = 0.7631\ \mathrm{m\,s^{-1}}$ from (3.2).

https://doi.org/10.1017/jfm.2025.10834 Published online by Cambridge University Press

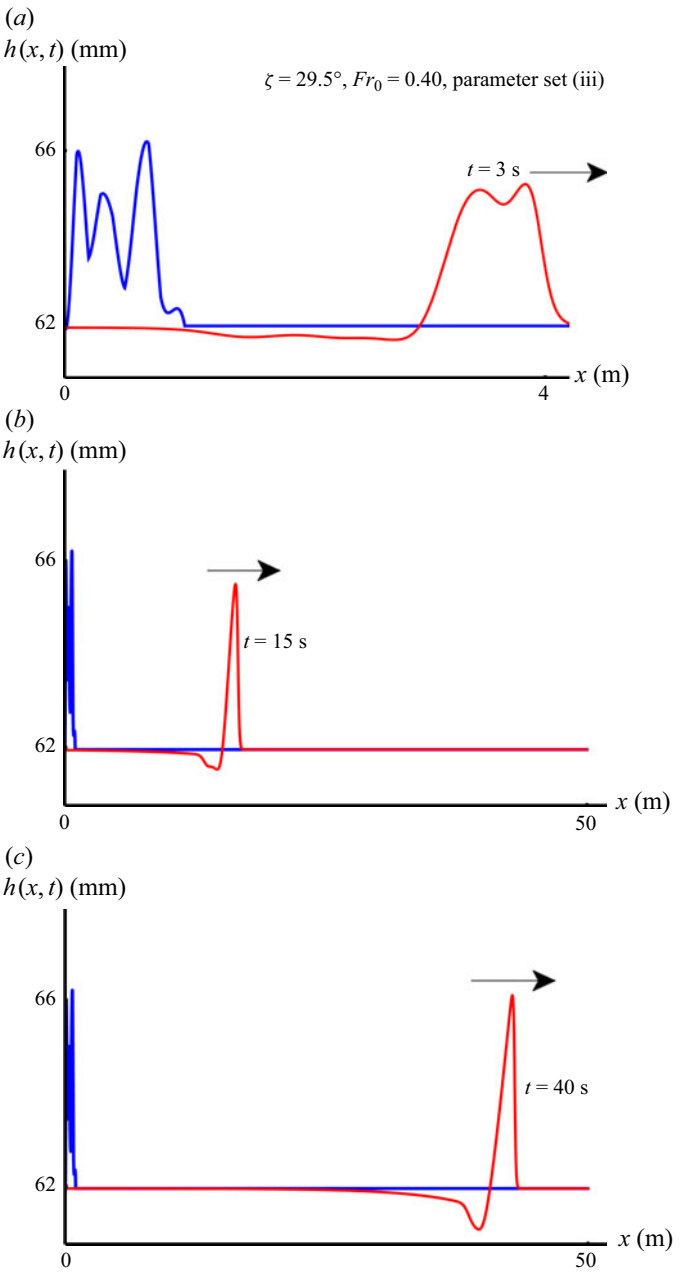


Figure 5. Numerical experiment for the same inclination angle $\zeta = 29.5°$ as in figure 4, but at a higher Froude number $Fr_0 = 0.40$. The initial condition (blue) is again as in the previous figures, only scaled up to match the increased height of the base flow. The red profiles are snapshots at (*a*) $t = 3$ s, (*b*) $t = 15$ s and (*c*) $t = 40$ s. Importantly, and in contrast to what we witnessed in figure 4, the solitary wave does not decay, but instead shows a tendency to grow.

Importantly, there is no sign of any hump developing at the trailing edge of this valley, thanks to the strong diffusion brought about by the increased value of $\nu(\zeta)$. The only undesirable feature of the solitary wave, created in the simulation of figure 4, is the fact

https://doi.org/10.1017/jfm.2025.10834 Published online by Cambridge University Press

that its amplitude gradually decreases as it travels downstream. Evidently, the enhanced diffusion also takes its toll on this first wave.

By increasing the value of Fr_0, thus boosting the energy content of the flow, one may compensate the attenuation of the amplitude. Figure 5 shows the series of events for $Fr_0 = 0.40$ (significantly higher than the value $Fr_0 = 0.15$ of figure 4), starting from the same initial condition used throughout, adequately scaled up to comply with the higher values of h_0 and $\bar{u}_0$. In figure 5(*a*), at $t = 3$ s, the situation is comparable to that of figure 4(*a*), but it is already apparent that the hilly pattern travels faster and that it sweeps up more material from the base flow, leaving an extended depression zone in its wake. In figure 5(*b*), at $t = 15$ s, this trend continues. A relatively deep valley has formed behind the front runner, which by now has attained the shape of a roll wave, travelling markedly faster than its counterpart in figure 4(*b*); at $t = 15$ s, it is already crossing the 16 m mark, whereas the front runner in figure 4(*b*) was at 12 m after the same time span.

In figure 5(*c*), at $t = 40$ s, the amplitude of the front runner is seen to grow, showing that the higher Froude number Fr_0 (i.e. the increased kinetic energy of the base flow) has more than compensated the diffusive effects. The growth in amplitude also means that the front runner is gaining speed. At the moment depicted here, its height is $h_p = 66.08$ mm and its speed is measured to be $1.0589\,\mathrm{m\,s^{-1}}$, again very close to the predicted value $c(h_p) = 1.0546\,\mathrm{m\,s^{-1}}$ from (3.2). While it is true that the solitary wave is carving a rather deep valley in its wake (much deeper than that for the solitary wave in figure 4*c*), this is of minor importance as long as no new waves are developed at the trailing edge.

The wave of figure 5(*c*) is precisely what we wanted to generate: a solitary wave in granular chute flow. Had the numerical simulation been carried out over longer times and distances, it is conceivable that eventually some small protrusion might appear at the trailing edge and that this would ultimately develop into a second wave. Yet, for a chute of 50 m, which is already very long for laboratory standards, the front runner remains solitary for its entire course. To illustrate this point and to highlight the successful generation of the (slowly growing) granular solitary wave of figure 5, supplementary movie 1 shows the temporal evolution of the numerical experiment in question.

4. Effect of varying the system parameters

4.1. *Varying the inclination angle, the Froude number and the initial condition*

There are three main parameters that govern the evolution of the initial perturbation: (i) the inclination angle of the chute; (ii) the Froude number of the carrying flow; and (iii) the mass of the granular material contained in the initial perturbation. In the present section, we have a closer look at these three parameters, by varying one of them at a time while keeping the other two constant.

The first parameter we will vary is the inclination angle ζ. From the numerical experiments of the previous section, it has become clear that to suppress any secondary waves in the wake of the front runner, ζ should be chosen close to – i.e. only marginally larger than – the angle of repose ζ_1. To make this observation quantitative, we take the value of $Fr_0 = 0.40$ and the initial perturbation of figure 5, and increase the value of ζ in small steps.

In figure 5, we took the very sharp value $\zeta = 29.5°$. Now, in figure 6, for $\zeta = 29.8°$, $29.9°, \ldots, 30.3°$, we check the shape of the profile that has emerged after 40 s. Naturally, the increase in ζ is accompanied by a decrease in the value h_0 in accordance with (2.8). Also, it is accompanied by a decrease of the diffusion parameter $\nu(\zeta)$ – as illustrated in figure 2 – and therefore, the secondary waves are less effectively suppressed, or in other

https://doi.org/10.1017/jfm.2025.10834 Published online by Cambridge University Press

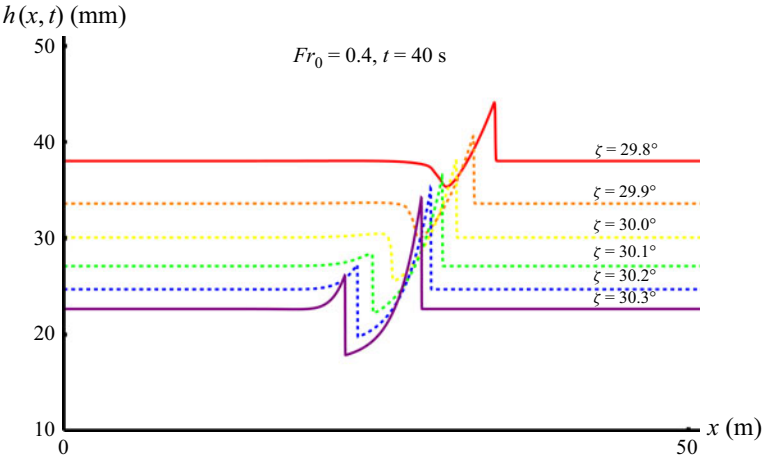


Figure 6. Six numerical simulations of the flow with fixed $Fr_0 = 0.40$ and varying inclination angle ζ, illustrating the effect of the latter on the shape of the resulting wave pattern after 40 s. For ζ close to the angle of repose ζ_1, the enhanced influence of the diffusion suppresses the formation of all waves but the front runner, which thus emerges as a solitary wave. By increasing the inclination angle, and hence weakening the diffusion, a second wave is allowed to rear its head in the wake of the front runner, violating thus its solitary nature.

words, the relative importance of the inertial terms on the left-hand side of the momentum balance equation (2.3) increases.

For $\zeta = 29.8°$ and also for $\zeta = 29.9°$, we observe that the profile after 40 s still shows just one travelling peak, but for $\zeta = 30.0°$, a small hump is visible at the rear end of the valley behind this front runner. The hump in question becomes increasingly pronounced for higher values of ζ and at $\zeta = 30.3°$, it has taken the form of a second roll wave, with its characteristic steep front and long tail. In contrast to what one might expect, we note that the speeds at which the peaks travel decrease with growing ζ. This is because we keep Fr_0 fixed and thus – in accordance with (2.8) – the values h_0 and $\bar{u}_0$ diminish as a function of ζ. The drop in h_0 also means that the granular layer on which the roll waves now form is considerably thinner, and hence their peaks do not reach quite as high any more. Indeed, h_p for the two roll waves at $\zeta = 30.3°$ is lower than the height of the corresponding waves at all smaller values of ζ ($\zeta = 29.8°, \ldots, 30.2°$). The decreased values of $\bar{u}_0$ and h_p result in a lower wave speed $c(h_p)$, as given by (3.2).

The second parameter we vary is the Froude number of the base flow, Fr_0. In figure 7, we show three representative simulations, at a fixed value of $\zeta = 29.7°$ and for the same initial condition we have used throughout, proportionally scaled with h_0. The first simulation (blue curves) are for $Fr_0 = 0.13$, close to the minimum value $\beta_* = 0.11$, but still allowing for fully dynamic flow. For this value of Fr_0, we observe that a solitary wave is formed, which however slowly decays over time, as evidenced by the two snapshots at $t_1 = 30$ s (dashed) and $t_2 = 40$ s (solid).

In the second simulation (orange curves), we have raised the value of Fr_0 to 0.50, i.e. we increase the energy content of the flow and thereby the values of h_0 and $\bar{u}_0$. As a result, the solitary wave is now seen to grow with time. It also carves out a considerably deeper valley. It may be inferred that there exists a certain value of Fr_0 between 0.13 and 0.50 for which the solitary wave would neither decay nor grow on the given time interval between t_1 and t_2. In that case, the diffusion (controlled via ζ) and the energy input (controlled via Fr_0) would exactly balance each other. This balance, however, is difficult to pinpoint since it is quite insensitive to changes in Fr_0. In experiments, on a finite chute, a perfectly balanced

https://doi.org/10.1017/jfm.2025.10834 Published online by Cambridge University Press

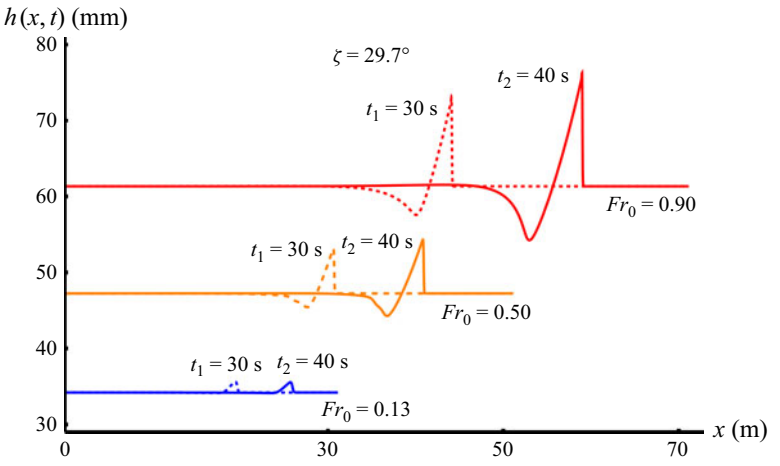


Figure 7. Three numerical experiments with constant inclination angle $\zeta = 29.7°$ (close to the angle of repose $\zeta_1 = 29.0°$) showing the influence of the Froude number Fr_0 on the front runner. In each experiment, two snapshots are presented, the first at $t_1 = 30$ s and the second at $t_2 = 40$ s. For $Fr_0 = 0.13$ (just exceeding $\beta_* = 0.11$), the peak height of the produced solitary wave diminishes very gradually (indiscernible on the scale of the figure). In contrast, for $Fr_0 = 0.50$, a slight gain in peak height can already be observed. Finally, for $Fr_0 = 0.90$, due to the further increase of the energy content of the flow, a mild upheaval, heralding the formation of a second roll wave, can be witnessed for $t_2 = 40$ s at the rear end of the valley behind the front runner.

solitary wave will be almost indistinguishable from a slowly varying one. For example, in the simulation at hand, with $Fr_0 = 0.50$, the growth in amplitude is merely 1.2 mm between t_1 and t_2, during which the wave has travelled more than 10 m along the chute. For all practical purposes, therefore, this solitary wave is very close to a steady waveform.

In the third simulation of figure 7 (red curves), with $Fr_0 = 0.90$, the growth has become more visible. Here, the amplitude of the front runner increases with 3.3 mm between t_1 and t_2, during which the wave has propagated 15 m. In this case, at t_2, we also observe that a second hump has started to form at the trailing end of the valley, so the front runner is not really solitary any more – although it would be quite challenging to recognise this in a laboratory experiment. For larger values of Fr_0 (especially at somewhat higher values of ζ), this second hump becomes more pronounced and eventually – on a very long chute – a whole train of roll waves will develop. This illustrates that one should not make Fr_0 too large, at the cost of violating the solitary nature of the front runner.

The third crucial parameter for generating a solitary wave is the amount of mass contained in the initial perturbation. In the simulations thus far, we have – for reasons of easy comparison – invariably used the same shape of the initial profile, only scaled up or down in proportion to h_0, and always keeping the normalised enclosed area of the perturbation fixed. The specific shape of the perturbation is in fact quite immaterial, since it only affects the transient stages but not the final waveform that emerges. The perturbation's size, however, is important. If insufficient material is added to the uniform base flow, the strong diffusion (for ζ close to the angle of repose) will gradually smear out the upheaval and eventually make it disappear – even if Fr_0 exceeds the critical value for the onset of the roll wave instability. One needs a sizeable perturbation to generate a sustainable solitary wave. This is illustrated in figure 8 for two perturbations with the same one-humped Gaussian shape but different sizes.

In figure 8(*a*,*b*), the initial Gaussian hump (blue curve) has exactly the same area as the initial perturbation in figure 5. In this case, the resulting waveform after 40 s is seen to be identical (both in amplitude and in wave speed) to the solitary wave of figure 5(*c*).

https://doi.org/10.1017/jfm.2025.10834 Published online by Cambridge University Press

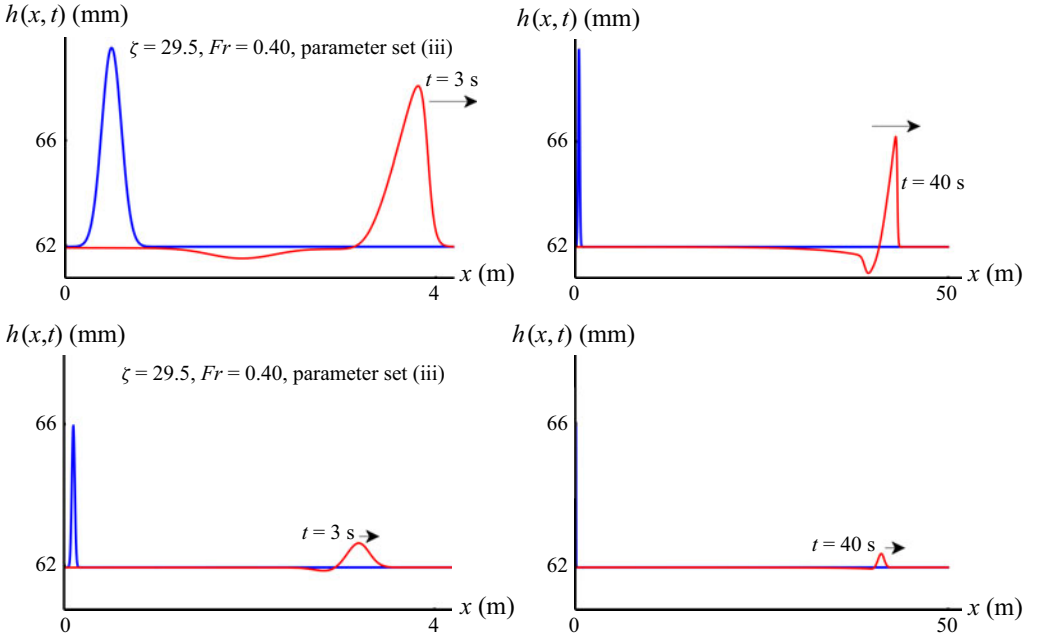


Figure 8. Snapshots of the temporal evolution, for $t = 3$ s and $t = 40$ s, of two Gaussian initial conditions (blue) with different areas. (*a*,*b*) The enclosed area of the blue curve above h_0 is exactly the same as in figure 5. Despite the notably different shape of the initial perturbation, the resulting solitary wave (at $t = 40$ s) is the same – both in shape and wavespeed – as that of figure 5(*c*), illustrating the fact that the ripened solitary waves are insensitive to the specific shape of the initial condition. (*c*,*d*) The area of the initial perturbation (blue) is a mere 8 % of that in panel (*a*,*b*). We observe the formation of a small solitary wave propagating down the chute with diminishing peak height, which will eventually vanish altogether. The inclination angle $\zeta = 29.5°$ and $Fr_0 = 0.40$ have been kept fixed at the same values as in figure 5 for ease of comparison.

This corroborates our earlier claim that the size – not the shape – of the initial perturbation is the factor that counts. We note that at $t = 3$ s, the amplitude of the hump has diminished (though not its area, which is increasing at the expense of the base flow as evidenced by the appearance of a trailing valley), while at 40 s, it is slowly growing, just as in figure 5(*c*). This illustrates that the formation of the solitary wave is not a monotonic process; between $t = 3$ s (figure 8*a*) and $t = 40$ s (figure 8*b*), it has passed through a transient phase where its amplitude was minimal.

The initial perturbation in figure 8(*c*,*d*) contains only 8 % of the material compared with its counterpart in figure 5, and we see that this is insufficient. The hump survives for a while yet never assumes the characteristic shape of a roll wave, and is slowly but surely smothered by the strong diffusion at this value of $\zeta = 29.5°$. At $t = 40$ s, it has already diminished drastically in size.

4.2. *Investigating other experimental set-ups*

Throughout the paper, we have illustrated the proposed method of generating a granular solitary wave by simulations employing the system parameters of table 1, set (iii), which corresponds to sand flowing on a chute with glass beads glued on its bed (Rocha *et al.* 2019; Edwards *et al.* 2023). In the present subsection, we perform simulations for the other two parameter sets of table 1 to check whether the method also works for different experimental set-ups.

https://doi.org/10.1017/jfm.2025.10834 Published online by Cambridge University Press

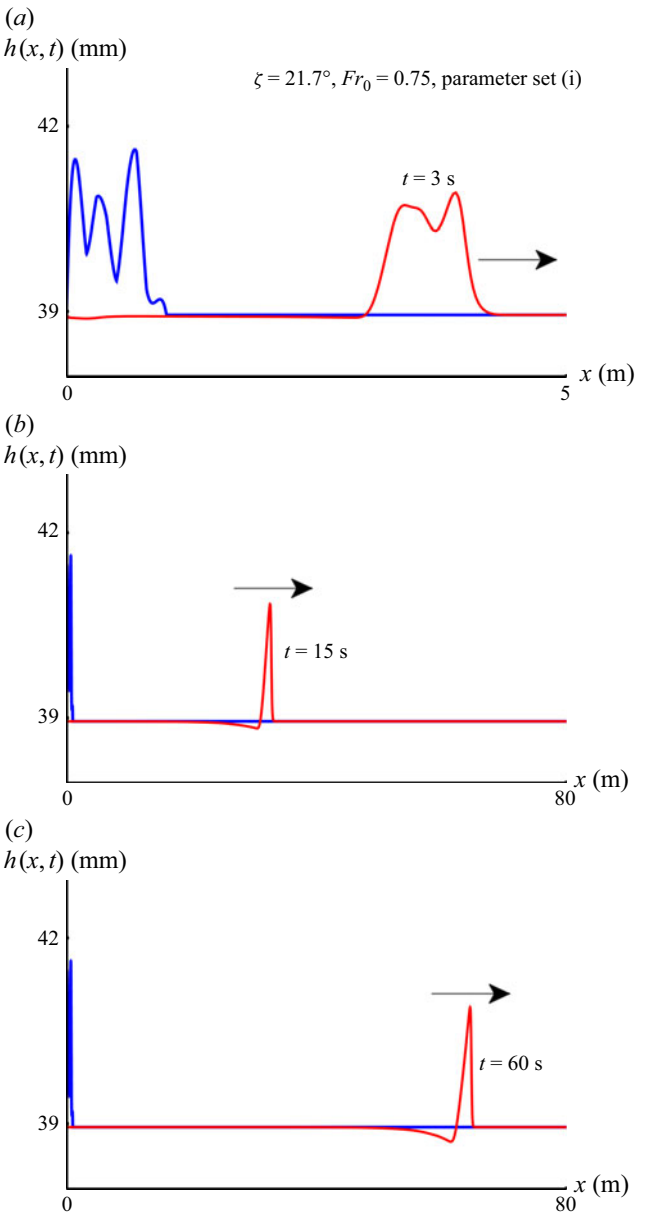


Figure 9. Three stages of the formation of a granular solitary wave at (*a*) $t = 3$ s, (*b*) $t = 15$ s, (*c*) $t = 60$ s for glass beads flowing over a bed of the same material (set (i) of table 1). The inclination angle $\zeta = 21.7°$ is just above ζ_1 and the Froude number of the base flow is $Fr_0 = 0.75$. The initial condition (blue) is the same as in all previous figures (except figure 8), only adjusted to the different height of the base flow.

The first check concerns the parameter set (i), corresponding to the flow of glass beads over a bed of glued glass beads (Russell *et al.* 2019). A representative simulation for this set-up is presented in figure 9. It is seen that, if ζ is chosen close to the minimal value ($\zeta_1 = 21.3°$) and Fr_0 is adjusted appropriately to counterbalance the mitigating effect of the strong diffusion, we again observe the formation of a slowly growing solitary wave.

Its dimensions are clearly different from those of figure 5, yet qualitatively, the features are the same. Also, the wave speed agrees excellently with the prediction of (3.2).

https://doi.org/10.1017/jfm.2025.10834 Published online by Cambridge University Press

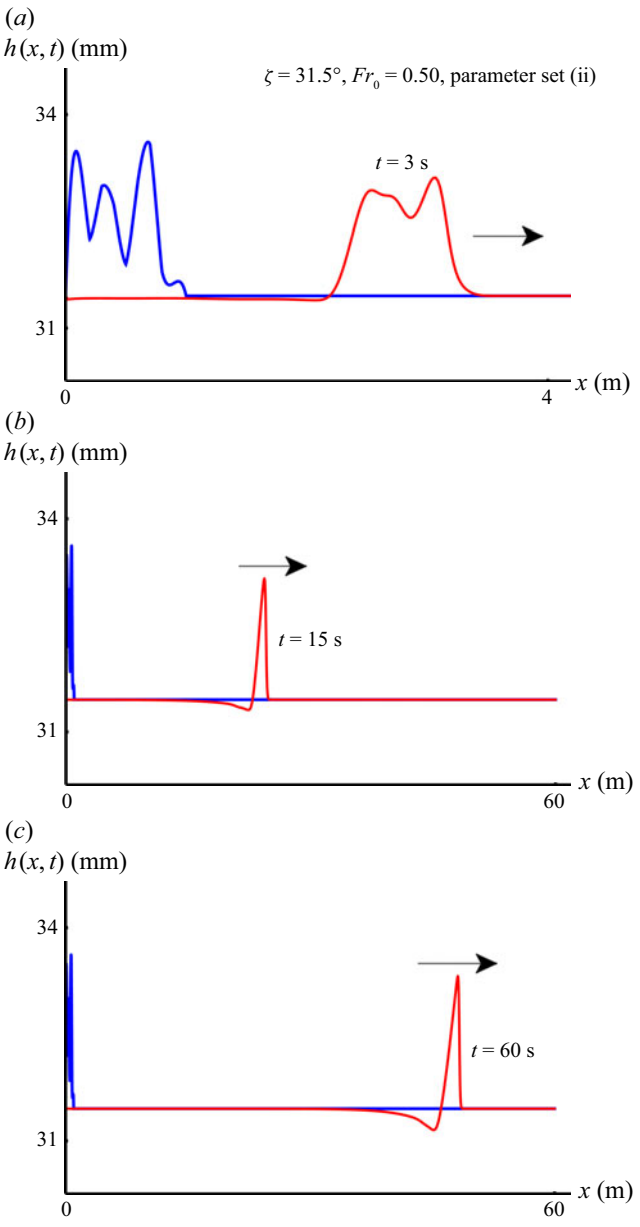


Figure 10. Successive stages of the formation of a granular solitary wave at (*a*) $t = 3$ s, (*b*) $t = 15$ s, (*c*) $t = 60$ s for carborundum particles flowing over a bed of glass beads (parameter set (ii) of table 1). The inclination angle is $\zeta = 31.5°$ and the Froude number of the base flow is $Fr_0 = 0.50$. The initial condition (blue) is the same as in all previous figures (except figure 8), properly scaled to be compatible with the height of the base flow.

For the solitary wave depicted in figure 9(*c*), with $h_0 = 38.95$ mm and peak height $h_p = 40.87$ mm, the measured speed is $1.0667\ \mathrm{m\,s^{-1}}$, whereas the analytical prediction gives $c(h_p) = 1.0647\ \mathrm{m\,s^{-1}}$.

Our final check is for the parameter set (ii) of table 1, corresponding to the flow of carborundum particles, again on a bed of glued glass beads (Edwards *et al.* 2017). In this case, the minimum inclination angle of the chute is $\zeta_1 = 31.1°$. By choosing the actual

https://doi.org/10.1017/jfm.2025.10834 Published online by Cambridge University Press

angle ζ close to that value ($\zeta = 31.5°$), and tuning Fr_0 appropriately, we once more observe the generation of a – slowly growing – granular solitary wave, see figure 10.

Regarding the speed of this wave, with base height $h_0 = 31.45$ mm and peak height $h_p = 33.31$ mm, we measure a speed of 0.7943 m s^{-1}. As in all our simulations, this agrees very well with the analytical prediction of (3.2), which yields $c(h_p) = 0.7921$ m s^{-1}.

All in all, as evidenced by the above-mentioned simulations, the proposed method for generating granular solitary waves is a very robust one. Additionally, it is generic in the sense that it is not restricted to a particular granular material or laboratory set-up.

5. Concluding remarks

In this study, we have introduced a new method for generating granular solitary roll waves on a chute, a waveform that until now had remained relatively unexplored (Razis *et al.* 2019; Kanellopoulos *et al.* 2022). The proposed method is based on numerical simulations of the generalised Saint-Venant equations for dry granular matter, using an initial condition that mimics a localised perturbation at the inlet of the chute.

Naturally, the Froude number of the incoming base flow (Fr_0) must exceed the critical value for which the uniform flow becomes unstable and susceptible to the formation of roll waves. The creation of the solitary wave is then achieved by choosing the inclination angle of the chute (ζ) close to the angle of repose, which strongly enhances the diffusive effects in the flow and hence suppresses the formation of any waves apart from the front runner. To not suppress the front runner as well, the Froude number Fr_0 should be taken well above the critical value – i.e. the energy injected into the flow must be sufficient – and the extra mass contained in the initial perturbation must be enough to create a sizeable roll wave.

An extensive parameter study has shown that, in particular, the choice of the inclination ζ is crucial, since the diffusion must be strong enough to quell the usual tendency of the flow to give birth to a whole series of roll waves. Once that has been accomplished, the method does not require too much fine-tuning of the Froude number (Fr_0) or of the excess mass contained in the initial perturbation; all that is needed is that these are sufficiently large to make the front runner viable and support its development into a self-sustaining (and typically even gradually growing) solitary wave. One of the things that transpired from our parameter study was that the precise shape of the initial perturbation did not matter: as long as the excess mass contained in it was sufficient, the flow always organised itself spontaneously in the form of a solitary roll wave.

The solitary wave thus generated is not a steady wave in the mathematical sense, but still evolving. We usually choose the parameters such that the wave is slowly growing. In that case, also the valley that it carves out will slowly expand, because the mass in the system is conserved and hence the wave can only grow at the expense of the carrying flow.

In all our simulations, we found excellent agreement between the measured speed of the peak of the solitary wave and the analytical prediction of the wave speed given by (3.2).

Finally, we have checked the proposed method for all three parameters sets of table 1, which correspond to actual experiments with different granular materials and set-ups. By choosing the inclination ζ close to the minimal value and by appropriately adjusting Fr_0 and the amount of mass contained in the initial perturbation, we were each time able to generate a solitary wave. Naturally, the amplitude and speed of the waves generated differed between the various parameter sets (note the different scales of the axes in figures 5, 9 and 10), yet the qualitative features were found to be always the same.

https://doi.org/10.1017/jfm.2025.10834 Published online by Cambridge University Press

We conclude that the described method is a generic one, not restricted to a particular granular material or experimental set-up. It is also robust in the sense that it does not require excessive fine-tuning of the key parameters. Thus, we are optimistic that the experimental verification of this way of generating granular solitary waves will prove to be straightforward and fairly easy to implement.

Supplementary movie. Supplementary movie is available at https://doi.org/10.1017/jfm.2025.10834.

Funding. The research conducted by G.K. is co-financed by the funding programme 'MEDICUS' of the University of Patras. D.R. is supported by the Sectoral Development Program (SDP 5223471) of the Ministry of Education, Religious Affairs and Sports, through the National Development Program (NDP) 2021-25, Grant No. 200/1029.

Declaration of interests. The authors report no conflict of interest.

References

Baker, J.L., Barker, T. & Gray, J.M.N.T. 2016 A two-dimensional depth-averaged $\mu(I)$-rheology for dense granular avalanches. *J. Fluid Mech.* **787**, 367–395.

Brock, R.R. 1967 Development of roll waves in open channels. PhD thesis, California Institute of Technology.

Di Cristo, C., Iervolino, M., Vacca, A. & Zanuttigh, B. 2009 Roll-waves prediction in dense granular flows. *J. Hydrol.* **377**, 50–58.

Edwards, A.N. & Gray, J.M.N.T. 2015 Erosion-deposition waves in shallow granular free-surface flows. *J. Fluid Mech.* **762**, 35–67.

Edwards, A.N., Rocha, F.M., Kokelaar, B.P., Johnson, C.G. & Gray, J.M.N.T. 2023 Particle-size segregation in self-channelized granular flows. *J. Fluid Mech.* **955**, A38.

Edwards, A.N., Russell, A.S., Johnson, C.G. & Gray, J.M.N.T. 2019 Frictional hysteresis and particle deposition in granular free-surface flows. *J. Fluid Mech.* **875**, 1058–1095.

Edwards, A.N., Viroulet, S., Johnson, C.G. & Gray, J.M.N.T. 2021 Erosion-deposition dynamics and long distance propagation of granular avalanchess. *J. Fluid Mech.* **915**, A9.

Edwards, A.N., Viroulet, S., Kokelaar, B.P. & Gray, J.M.N.T. 2017 Formation of levees, troughs and elevated channels by avalanches on erodible slopes. *J. Fluid Mech.* **823**, 278–315.

Fei, J., Jie, Y., Xiong, H. & Wu, Z. 2021 Granular roll waves along a long chute: from formation to collapse. *Powder Technol.* **377**, 553–564.

Forterre, Y. 2006 Kapiza waves as a test for three-dimensional granular flow rheology. *J. Fluid Mech.* **563**, 123–132.

Forterre, Y. & Pouliquen, O. 2003 Long-surface-wave instability in dense granular flows. *J. Fluid Mech.* **486**, 21–50.

GDR-MiDi 2004 On dense granular flows. *Eur. Phys. J. E* **14**, 341–365.

Gray, J.M.N.T. & Cui, X. 2007 Weak, strong and detached oblique shocks in gravity driven granular free-surface flows. *J. Fluid Mech.* **579**, 113–136.

Gray, J.M.N.T. & Edwards, A.N. 2014 A depth-averaged $\mu(I)$-rheology for shallow granular free-surface flows. *J. Fluid Mech.* **755**, 503–534.

Hamdi, S., Schiesser, W.E. & Griffiths, G.W. 2007 Method of lines. *Scholarpedia* **2**, 2859.

Johnson, C.G. & Gray, J.M.N.T. 2011 Granular jets and hydraulic jumps on an inclined plane. *J. Fluid Mech.* **675**, 87–116.

Kanellopoulos, G. 2021 The granular monoclinal wave: a dynamical systems survey. *J. Fluid Mech.* **921**, A6.

Kanellopoulos, G. 2025 Formation of standing waves in granular chute flows induced by mild basal topography. *J. Non-Newton. Fluids* **343**, 105453.

Kanellopoulos, G., Razis, D. & van der Weele, K. 2021 On the structure of granular jumps: the dynamical systems approach. *J. Fluid Mech.* **912**, A54.

Kanellopoulos, G., Razis, D. & van der Weele, K. 2022 On the shape and size of granular roll waves. *J. Fluid Mech.* **950**, A27.

Kanellopoulos, G., Razis, D. & van der Weele, K. 2024 Pairwise balancing of forces in traveling granuler waves. *Physica D* **469**, 134324.

Pouliquen, O. & Forterre, Y. 2002 Friction law for dense granular flows: application to the motion of a mass down a rough inclined plane. *J. Fluid Mech.* **453**, 113–151.

https://doi.org/10.1017/jfm.2025.10834 Published online by Cambridge University Press

RAZIS, D., EDWARDS, A.N., GRAY, J.M.N.T. & VAN DER WEELE, K. 2014 Arrested coarsening of granular roll waves. *Phys. Fluids* **26**, 123305-1–123305-25

RAZIS, D., KANELLOPOULOS, G. & VAN DER WEELE, K. 2018 The granular monoclinal wave. *J. Fluid Mech.* **843**, 810–846.

RAZIS, D., KANELLOPOULOS, G. & VAN DER WEELE, K. 2019 A dynamical systems view of granular flow: from monoclinal flood waves to roll waves. *J. Fluid Mech.* **869**, 143–181.

RAZIS, D., KANELLOPOULOS, G. & VAN DER WEELE, K. 2023 Roll waves as relaxation oscillations. *Phys. Fluids* **35**, 63333.

ROCHA, F.M., JOHNSON, C.G. & GRAY, J.M.N.T. 2019 Self-channelisation and levee formation in monodisperse granular flows. *J. Fluid Mech.* **876**, 591–641.

RUSSELL, A.S., JOHNSON, C.G., EDWARDS, A.N., VIROULET, S. & GRAY, J.M.N.T. 2019 Retrogressive failure of a static granular layer on an inclined plane. *J. Fluid Mech.* **869**, 313–340.

SAVAGE, S.B. & HUTTER, K. 1989 The motion of a finite mass of granular material down a rough incline. *J. Fluid Mech.* **199**, 177–215.

SCHIESSER, W.E. 1991 *The Numerical Method of Lines: Integration of Partial Differential Equations*. Academic Press.

VIROULET, S., BAKER, J.L., EDWARDS, A.N., JOHNSON, C.G., GJALTEMA, C., CLAVEL, P. & GRAY, J.M.N.T. 2017 Multiple solutions for granular flow over a smooth two-dimensional bump. *J. Fluid Mech.* **815**, 77–116.

VIROULET, S., BAKER, J.L., ROCHA, F.M., JOHNSON, C.G., KOKELAAR, B.P. & GRAY, J.M.N.T. 2018 The kinematics of bidisperse granular roll waves. *J. Fluid Mech.* **848**, 836–875.

YOP, P., FORTERRE, Y. & POULIQUEN, O. 2005 Crucial role of sidewalls in granular surface flows: consequences for the rheology. *J. Fluid Mech.* **541**, 167–192.

YOP, P., FORTERRE, Y. & POULIQUEN, O. 2006 A constitutive relation for dense granular flows. *Nature* **44**, 727–730.

YU, B. & CHU, V.H. 2022 The front runner in roll waves produced by local disturbances. *J. Fluid Mech.* **932**, A42.

https://doi.org/10.1017/jfm.2025.10834 Published online by Cambridge University Press